A coarse-grained approach to modeling gas transport in swelling porous media

Jian Wu [a], Yixiang Gan [a,b], Pengyu Huang [c], Luming Shen [a,*]

[a] *School of Civil Engineering, The University of Sydney, NSW, 2006, Australia*
[b] *Sydney Nano Institute, The University of Sydney, NSW, 2006, Australia*
[c] *CSIRO Mineral Resources, QCAT, 1 Technology Court, Pullenvale, QLD, 4069, Australia*

ARTICLE INFO

ABSTRACT

In many engineering applications, understanding gas adsorption and its induced swelling in nanoporous materials is crucial. In this study, we propose a novel coarse-grained molecular dynamics (CGMD) model with gas-gas, solid-solid, and gas-solid interactions explicitly controlled to achieve the coupling between gas transport and solid deformation at the microscale. The CGMD model has the capability to recover solid and gas properties, including density, Young's modulus of the solid, and viscosity of the gas to generate a broad range of swelling ratios relevant to nanostructures by using the innovative bead-spring chain networks. A comparison is made between gas transport through deformable and non-deformable nanochannels of varying sizes (35.4–123.9 nm), which is also compared with the macroscopic Hagen-Poiseuille equation. The proposed model has been further tested in a simplified nanoporous medium composed of four randomly distributed spherical solids. The Kozeny-Carman equation can generally describe the relationship between permeability and porosity, but small deviations are observed in the case of swelling porous media. Our results justify the effect of swelling on reducing gas permeability and provide a new approach to modeling gas transport in swelling porous media at the microscale within the framework of CGMD, with potential applications spanning nanofluidics, energy storage technologies, and environmental nanotechnology.

1. Introduction

Porous materials such as soils, organic matter, and gels exhibit the capacity to deform when exposed to thermal, mechanical, or chemical triggers. Applications of fluid flow in swelling porous media encompass a variety of fields and scenarios. For instance, porous coffee particles are wetted through imbibition during the brewing process, which can induce swelling and affect the extraction kinetics of coffee.[1,2] In nanotechnology, understanding the effect of swelling on structural and transport properties helps optimize the performance of membranes and hydrogels for aqueous separation and drug delivery applications.[3,4] In petroleum engineering, understanding fluid flow through swelling porous rocks is vital for enhanced oil and gas recovery because rock swelling can impact the difficulty with which oil and gas are extracted from a reservoir.[5,6] In carbon sequestration, the injected CO_2 enters the rock matrix as an adsorbed phase, generating internal stress and decreasing the reservoir permeability and gas injectivity.[7–9] Due to the difficulty in capturing fluid-solid interactions at mobile boundaries, the

coupling effect between fluid flow and solid deformation in porous media is rarely studied in the literature. It is indispensable to develop novel and straightforward numerical models to investigate fluid flow through swelling porous media to address these real-life problems described above.

A variety of numerical approaches have been implemented in studying fluid flow through deformable porous media. Mou and Chen[10] coupled the immersed boundary (IB) condition with the lattice Boltzmann method (LBM) and introduced a spring constant to consider the solid deformation effects. Their results show that fluid flow is more complex and flow resistance increases in highly deformable porous media. Matias et al.[2] implemented continuous boundary changes using fluid, solid, and interface nodes in LBM to investigate fluid flow subject to both solid swelling and erosion. Mo et al.[1] proposed a smoothed particle hydrodynamics (SPH) model to simulate water filtration through coffee particles. The model considers the coupling between particle swelling and intraparticle diffusion of water. Each coarse coffee particle comprises many subsized particles connected by harmonic

---

* Corresponding author.
E-mail address: luming.shen@sydney.edu.au (L. Shen).

bonds and swells as the bond length increases as a function of water concentration. It is found that swelling mainly affects interparticle flow, and its effect on intraparticle diffusion is nearly ignorable. Sweijen et al.[11] coupled a pore-scale fluid flow model to the discrete element method (DEM) to simulate unsaturated flow in deforming and swelling granular materials, where air invaded a packing of super absorbent polymer (SAP) particles as they absorb water and swell. Wu and Firoozabadi[12] used all-atomic molecular dynamics (MD) to investigate methane flow through a domain of kerogen matrix, which can swell upon adsorption at various gas pressures. The microstructural flexibility is found to constrain gas transport due to changes in pore shape.

Particle-based numerical methods such as MD are convenient in solving problems involving complex gas-solid interactions since no explicit boundary conditions are needed. In fact, MD has been widely adopted in studying multiphase/multicomponent flow,[13–17] adsorption, and adsorption-induced deformation.[3,18–20] However, this method is computationally expensive and usually requires a large number of atoms/molecules with small time steps. It is not feasible for simulating larger complex nanopore networks with a size of microns due to high computational cost. In larger and more complex systems, the heterogeneity of surfaces and the connectivity of pore networks can significantly impact gas transport and adsorption. Coarse-grained molecular dynamics (CGMD) overcomes such limits with the idea of mapping a group of atoms/molecules into a coarse-grained (CG) particle.[21] It can be extended to model mesoscopic multiphase and multicomponent fluid flow and transport in single pores and complex networks by calibrating force parameters to reproduce solid, fluid, and interfacial properties, allowing us to study the effects of geometrical factors, such as porosity, pore size, pore shape, and pore distribution.[22] Moreover, CGMD offers greater flexibility to efficiently calibrate these properties across different liquid-solid systems. This adaptability is particularly valuable when investigating various materials and conditions. For example, Huang et al.[23] developed a CGMD framework composed of morse potential, many-body dissipative particle dynamics (MDPD), and Lennard-Jones (LJ) potential to model multiphase interactions at the microscale, which can successfully recover static and dynamics contact angles in the CO_2-water-silica system.[24] Xia et al.[25] adopted MDPD to simulate complex two-fluid flow in nanoporous networks of shale constructed from FIB-SEM (focused ion beam scanning electron microscopy) images. Rao et al.[26] and Xia et al.[27] built a modified MDPD model to study hydrocarbon flow in amorphous silica cylindrical nanochannels and pore networks of packed silica nanoparticles. Despite the versatility of CGMD in the simulation of multiphase flow in porous media, the solid boundary particles are usually treated as static with no deformation considered in the flowing process.

The coupling between fluid flow and deformation in porous media can lead to changes in transport properties, which may cause concerns in many engineering practices. In this study, we focus on CO_2 injection into shale reservoirs and propose a novel CGMD model to simulate gas transport in deformable porous media induced by sorption. The model separately sets up gas-gas, solid-solid, and gas-solid interactions using different potential functions that are calibrated to represent gas and solid properties accurately. A bead-spring chain network model is used to describe the soft solid mimicking organic matter in shale, which has a low Young's modulus and high flexibility to swell. Sorption-induced swelling of solids is explicitly controlled to investigate its effect on gas permeability in slit pores and spherical porous media.

2. Computational methods

2.1. Potential functions for gas-solid system

Kerogen is solid, insoluble organic matter in sedimentary rocks such as shale.[28] In molecular simulations, a kerogen matrix is built by assembling dozens of kerogen macromolecule units through annealing and relaxing. It has a significantly lower stiffness compared to inorganic

minerals, with Young's modulus typically ranging from 1 to 10 GPa.[29] Upon adsorption, the adsorbed gas in kerogen pore space can impose stress on pore walls and induce the expansion of the porous structure.[30,31] In our CGMD approach, the solid is described by a bead-spring chain network model with both non-bonding and bonding potentials among CG particles, which is widely used to accurately capture the mechanical properties and swelling kinetics of microgel immersed in solvents.[32,33] The bonding potential is used for directly bonded CG particles, and the non-bonding potential is included if particle pairs are separated by ≥ 2 bonds or on different chains. Compared to the crystallized distribution of particles, the bead-spring chain networks also keep the amorphous structure of kerogen. The finite extensible nonlinear elastic (FENE) potential is used for the bonding interaction, consisting of an attractive term and an LJ repulsive term

$$E = -0.5KR_0^2 \ln\left[1 - \left(\frac{r}{R_0}\right)^2\right] + 4\varepsilon_s\left[\left(\frac{\sigma_s}{r}\right)^{12} - \left(\frac{\sigma_s}{r}\right)^6\right] + \varepsilon_s \quad (1)$$

where K is the bond stiffness, R_0 is the maximum extended bond length, and ε_s and σ_s are the LJ energy and distance parameters. The second term is cut off at the minimum of the LJ potential $2^{\frac{1}{6}}\sigma_s$. The non-bonding potential is expressed by a short-range LJ potential cut off at 2.5 σ_s.

$$E = 4\varepsilon_s\left[\left(\frac{\sigma_s}{r}\right)^{12} - \left(\frac{\sigma_s}{r}\right)^6\right] \quad (2)$$

The interaction among CG gas particles (i.e., CO_2) is characterized by the dissipative particle dynamics (DPD) force field, which comprises a conservative force F^C, a dissipative force F^D, and a random force F^R[34]

$$\boldsymbol{F} = \left(F^C + F^D + F^R\right)\boldsymbol{e}_{ij} \quad (3)$$

$$F^C = Aw(r) \quad (4)$$

$$F^D = -\gamma w^2(r)\left(\boldsymbol{e}_{ij} \bullet \boldsymbol{v}_{ij}\right) \quad (5)$$

$$F^R = \sigma w(r)\alpha(\Delta t)^{-\frac{1}{2}} \quad (6)$$

$$w(r) = 1 - \frac{r}{r_c} \quad (7)$$

where $\boldsymbol{e}_{ij}$ is the unit vector in the direction $\boldsymbol{r}_i - \boldsymbol{r}_j$, $\boldsymbol{v}_{ij}$ is the vector difference $\boldsymbol{v}_i - \boldsymbol{v}_j$, Δt is the timestep size, $w(r)$ is the weight function that varies between 0 and 1, and r_c is the pairwise cut-off. The amplitude σ, the Gaussian random variable α with zero mean and unit variance, and the viscous dissipation coefficient γ satisfy a fluctuation-dissipation theorem $\sigma = \sqrt{2k_BT\gamma}$. DPD uses a soft and purely repulsive interaction. It models a fluid that behaves like gas as CG particles are forced to move away from each other and occupy the entire computational domain.[35,36] By combining the attractive and repulsive interactions (such as MDPD), it is possible to simulate multiphase flow systems with liquid and gas co-existing and liquid-gas phase transitions.[37] The pressure-density dependence obtained in the DPD fluid has been reported to align with the van der Waals equation.[37] It is noted that the non-conservative part of the DPD force field (i.e., F^D and F^R) acts as a thermostat on pairwise interactions. Herein, a per-particle Nosé-Hoover thermostat is used to replace the dissipative and random forces with only the conservative part kept.[23,24] This technique allows easy control of solid and gas temperatures when modeling fluid flow and solid deformation simultaneously. Therefore, only two DPD parameters need to be calibrated to achieve agreements with the measured CO_2 density and viscosity.

The interaction between solid and gas CG particles is also modeled by the short-range LJ potential in Eq. (2), similar to all-atomic molecular dynamics. The cut-off distance is set as 2.5 σ_{gs}, where σ_{gs} is the LJ distance parameter between solid and gas CG particles. As the LJ potential

function's energy depth ε_{gs} is varied, the repulsive or attractive force contributions from gas to solid particles can be tuned, which turns into the volume change of the solid structure.

2.2. Model calibration

Simulations are run with all quantities being unitless. We first set up the three fundamental quantities based on Huang et al.[24]: mass $M = 7.29 \times 10^{-21}$ kg, energy $E = 5.53 \times 10^{-18}$ J, and distance $D = 3.54 \times 10^{-8}$ m. All the other given quantities can then be related to these three fundamental ones and reduced to unitless. In the text below, unitless parameters will be expressed with an asterisk * as the superscript. The coarse-grained model is implemented in the open-source molecular dynamics software LAMMPS.[38]

2.2.1. Gas density and viscosity

The calibration of CO_2 DPD parameters is referred from Huang et al.[24] A typical shale reservoir temperature at $T = 333.15$ K is chosen for the CG gas-solid system, which is assumed to be equivalent to $T^* = 1$. The DPD parameters are calibrated against density and viscosity values of CO_2 obtained from the US National Institute of Standards and Technology (NIST) webbook.[39] After an initial set of DPD parameters is chosen, the simulation box with only CG CO_2 particles is relaxed and the equilibrium density is measured. The reverse non-equilibrium molecular dynamics (rNEMD) algorithm of Muller-Plathe[40] is then implemented to calculate gas viscosity where momentum in the x-direction is swapped between particles in the upper and lower layers in the z-direction to generate a velocity gradient. The viscosity can be calculated from the momentum flux and the x-direction velocity gradient. After a series of trials, $m_g{}^* = 0.284$, $A^* = 44.1$, and $r_C{}^* = 0.63$ are selected to approximately recover the density and viscosity of CO_2 from 10 to 20 MPa and a large cut-off $r_C{}^* = 1.2$ is used for the lower pressure range at 2–10 MPa. Since phase transition is not considered in this study, the DPD model is not intended to capture the density data from vapor to supercritical state near 7.4 MPa. A factor of 0.2 is adopted to reduce the physical time unit so that the simulated viscosity in the CG system can match with NIST values.[24] As can be seen from Fig. 1, the calibrated DPD model shows a good fit with the NIST CO_2 density data when the pressure is 2–6 MPa and 14–20 MPa. However, the simulated pressure-dependent viscosity data is relatively uniform compared to the NIST curve. This suggests that the set of DPD parameters may need to be slightly adjusted for each pressure. This study only focuses on the gas transport at P = 15 MPa, as the maximum swelling associated with gas adsorption is expected at this pressure level.

2.2.2. Young's modulus of solid

The bead-spring solid model is calibrated against the experimental density and Young's modulus of kerogen through a trial-and-error method. Over 50 sets of bond parameters K, R_0 and LJ parameters ε_s,

σ_s have been tested out with four groups of chain length and bead number (i.e., 20 beads/chain × 500 chains, 40 × 250, 10 × 1000, 50 × 200). The sensitivity study shows that ε_s is the only parameter that has a strong positive correlation with Young's modulus, while the other three force parameters and chain properties all reveal weak correlations. This may be attributed to the fact that the non-bonding forces among chains predominantly control the solid strength. To create the initial bead-spring structure for the solid, 20 chains each containing 500 beads are randomly placed into a large simulation box to avoid crossing using the pre-processing chain tool in LAMMPS. As shown in Fig. 2a, the simulation box with the bead-spring solid structure is then relaxed into a condensed state at 300 K and 0 MPa, which has a density close to kerogen at 1249 kg/m³. The solid model is deformed in the x-direction at strain rates of 10^{-5}, 10^{-4}, and 10^{-3} per unit time with the lateral boundaries controlled under the NPT ensemble to maintain zero pressure. Young's modulus of the solid is calculated at 0.7–0.8 GPa by linear-fitting the stress-strain curve within the range of 1 % strain (Fig. 2b). This value is close to the lower limit of the reported Young's modulus of kerogen and gives ease to generate a wide range of swelling. After calibrating the gas and solid model parameters, swelling induced by gas adsorption can be measured by tuning the gas-solid interactions through the two LJ parameters σ_{gs} and ε_{gs}. The physical and unitless model parameters are provided in Table 1 along with their conversion relations.

3. Case studies of swelling and gas transport

3.1. Adsorption and swelling of a solid sphere

Once the proper range of density and Young's modulus has been determined for the solid, a spherical region is cut from the solid matrix and further relaxed. This spherical solid matrix is then immersed in pure gas at 15 MPa and equilibrated until its radius of gyration converges. Two pistons are placed on the left and right sides to maintain the gas pressure under the NVT ensemble. The surface adsorption amount is estimated by counting the number of CG gas particles that have a local gas density higher than the bulk one (~604 kg/m³) in OVITO.[41] The surface area of the solid is calculated from the constructed surface mesh using the alpha-shape method with a probing size of 1.5D, as shown in Fig. 3a. According to Fig. 3b, it can be seen that increasing the gas-solid interaction energy term $\varepsilon_{gs}{}^*$ results in more adsorbed gas particles, and the maximum adsorption amount increases with the increasing gas-solid LJ distance term $\sigma_{gs}{}^*$. However, a lower energy minimum is required to initiate the surface gas adsorption at small $\sigma_{gs}{}^*$. As the resolution is much lower in CGMD and each gas particle consists of hundreds or thousands of actual gas molecules, this measured surface adsorption amount is not directly comparable to MD results. Instead, a more practical way is to calculate the density distribution normalized by the bulk density and evaluate its effect on gas transport, which will be further discussed in the next section.
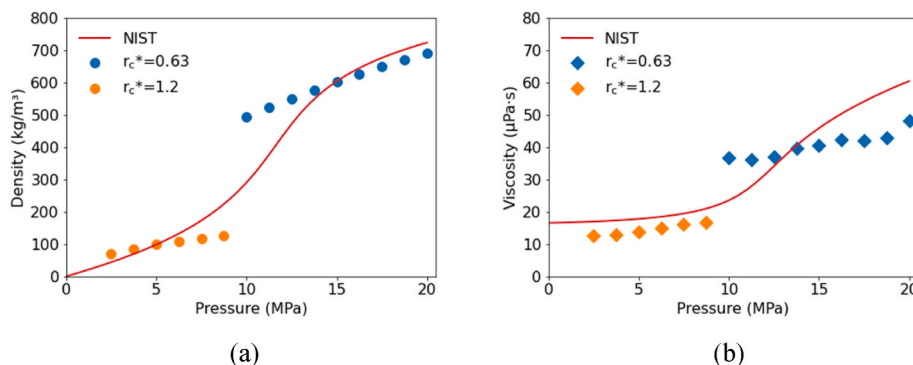

Fig. 1. Calibrated (a) density and (b) viscosity of CO_2 as a function of pressure at 333.15 K and comparison with NIST data.
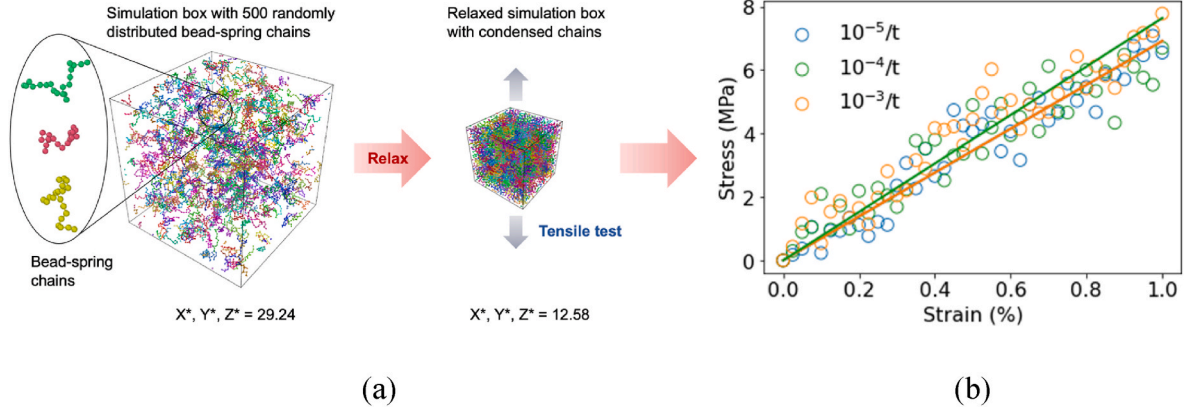
Fig. 2. (a) The construction process of the solid model using bead-spring chain networks and (b) its stress-strain curves under different strain rates in the x-direction. The colored solid lines are the linear fits for the corresponding data. The blue and green lines overlap. (For interpretation of the references to color in this figure legend, the reader is referred to the Web version of this article.)

Table 1
CG model parameters and conversion between dimensionless and real units.

Parameter	Physical value	Dimensionless value*	Conversion
Unit mass, M	7.29×10^{-21} kg	1	–
Unit energy, E	5.53×10^{-18} J	1	–
Unit distance, D	3.54×10^{-8} m	1	–
Unit time, t	2.57×10^{-10} s	1	$t^* = 0.2t\sqrt{\dfrac{E}{MD^2}}$
Solid-solid interaction (FENE and LJ)			
Solid particle mass, m_s	1.24×10^{-20} kg	1.7	$m_s^* = \dfrac{m_s}{M}$
Bond stiffness, K	2.04×10^6 N/m	9000	$K^* = \dfrac{KD^2}{E}$
Maximum extended bond length, R_0	7.08×10^{-8} m	2	$R_0^* = \dfrac{R_0}{D}$
LJ energy, ε_s	1.66×10^{-16} J	30	$\varepsilon_s^* = \dfrac{\varepsilon_s}{E}$
LJ distance, σ_s	2.12×10^{-8} m	0.6	$\sigma_s^* = \dfrac{\sigma_s}{D}$
CO_2-CO_2 interaction (DPD)			
Gas particle mass, m_g	2.07×10^{-21} kg	0.284	$m_g^* = \dfrac{m_g}{M}$
Repulsive force, A	2.82×10^{11} N	44.1	$A^* = \dfrac{AD}{E}$
Pairwise cut-off, r_c	2.23×10^{-8} m	0.63	$r_c^* = \dfrac{r_c}{D}$
Gas-solid interaction (LJ)			
LJ energy, ε_{gs}	$5.53\text{-}77.42 \times 10^{-18}$ J	1–14	$\varepsilon_{gs}^* = \dfrac{\varepsilon_{gs}}{E}$
LJ distance, σ_{gs}	$1.06\text{-}2.12 \, 10^{-8}$ m	0.3–0.6	$\sigma_{gs}^* = \dfrac{\sigma_{gs}}{D}$

The volumetric strain can be estimated from the initial and swollen radii of gyration assuming a cubic relationship between volume and radius. It is found that varying σ_{gs}^* and ε_{gs}^* can greatly impact the size of the solid, generating a wide range of swelling ratios up to 130 % under the pre-set conditions as shown in Fig. 3c. Different patterns are observed between swelling and ε_{gs}^* as σ_{gs}^* varies from 0.3 to 0.6. When $\sigma_{gs}^* = 0.3$, increasing the gas-solid interaction energy leads to a slight contraction of the spherical solid. A much greater swelling ratio is observed as σ_{gs}^* increases from 0.4 to 0.5 and above. This is because the LJ distance parameter between two solid CG particles is set at 0.6, close to the separation distance between CG gas particles. Assuming one CG gas particle lies in the middle between the two solid particles, the total interaction force will always be repulsive when the LJ distance between the gas-solid CG particles is larger than 0.3, which is half the LJ distance of solid CG particles. The repulsion becomes stronger as the gas-solid LJ distance further shifts to a higher value. A sigmoid relationship is found between swelling and ε_{gs}^* (ranges from 1 to 14) at both $\sigma_{gs}^* = 0.5$ and

0.6. By increasing this LJ energy parameter between gas and solid, the gas-solid interactions are more favored than solid-solid ones, resulting in the rapid growth of the solid size. However, in the late stage, such swelling behavior of the spherical solid gradually stabilizes as the distance between two solid particles is also limited by bonding interactions, which are much stronger than the LJ interactions. Fig. 3d shows that the swelling behavior is proportional to the surface adsorption amount, consistent with the conclusion in MD simulations.[42] Moreover, the same amount of adsorbed gas can induce higher swelling at larger σ_{gs}^*. The parametric study shows that tuning the gas-solid interactions within the CGMD framework can generate a wide range of solid swelling ratios, which can be used in gas flow simulations. The swelling curve at $\sigma_{gs}^* = 0.5$ is chosen for studying gas transport in the following sections, with calibrations and validations of the coupling system.

3.2. Gas transport through slit nanochannels

With the proper parameters determined for solid-solid, gas-gas, and gas-solid interactions, gas transport is first simulated in a slit nano-channel. As shown in Fig. 4a, two pistons with imposed forces are emplaced at the left and right ends of the channel in the x-direction to control the pressure of the two gas reservoirs. Pressure-driven flow can be generated after a pressure drop of 0.75 MPa is created between the left and right gas reservoirs, which have an average of 15 MPa. The dimensions of the system are $70 \times 12.59 \times 14.59$, or $2.5 \times 0.45 \times 0.52$ μm^3 in physical units. The effective slit pore size (Fig. 4b) ranges from 1 to 3.5 (i.e., 35.4–123.9 nm). It should be noted that the effective slit pore size is the pore width where the gas transport can take place and excludes the non-accessible zones defined by the gas-solid LJ interaction distance $\sigma_{gs}^* = 0.5$. Two sets of simulations are performed, in which the CG particles of the solid matrix are kept either mobile or immobile. A spring force is applied independently to each CG particle of the solid to tether it to its initial position, which is calculated as $-K_s r$, where r is the displacement of the particle from its current position to the position at $t = 0$. A small spring constant at $K_s^* = 10$ keeps the solid structure in place subject to gas transport but still deformable, while a large value at $K_s^* = 10,000$ makes the solid structure fully rigid and non-deformable. Different swelling ratios under gas transport can be obtained by tuning the gas-solid interaction energy ε_{gs}^*. The simulation timestep dt* is set at 0.0001 to ensure there is no atom missing and energy is conserved when running simulations in the NVE ensemble.

Velocity and density profiles within the slit nanochannel are obtained by the spatial binning method, where CG gas particles are assigned to multiple bins in the z-direction to obtain the bin-averaged properties. Time-averaged velocity and density can be further calcu-
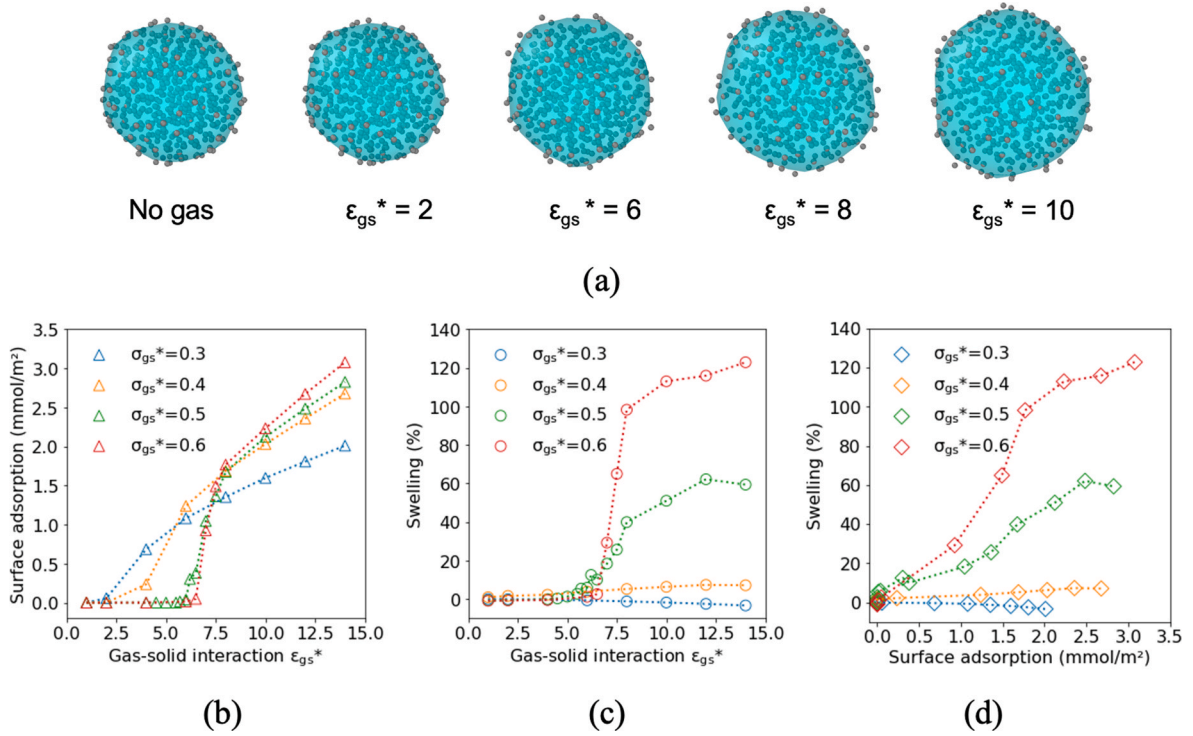
Fig. 3. (a) Swelling of a solid sphere immersed in CO_2 (gas phase not shown for clarity) with constructed surface mesh when ε_{gs}^* increases (P = 15 MPa, T = 333.15 K, $\sigma_{gs}^* = 0.5$). (b) Surface gas adsorption and (c) solid swelling ratio as a function of ε_{gs}^* when σ_{gs}^* varies. (d) Relationship between solid swelling ratio and surface gas adsorption amount.

lated from each bin after the gas transport has reached a steady state within 10^6 timesteps. The 2×10^6 - 3×10^6 timesteps are typically used for production with a sampling frequency of 10 timesteps. The parabolic curves are calculated from the Hagen-Poiseuille equation $v(z) = \frac{1}{2\mu}\frac{dP}{dx}(Hz - z^2)$, with the known quantities of pressure gradient (dP/dx), viscosity (μ), and effective pore size (H). A sensitivity analysis is performed on gas pressure between 13 and 17 MPa. With the calibrated parameters for 15 MPa, the measured gas flux through the slit pore stays nearly constant and is not significantly impacted by the pressure variations (Fig. S1 in the supplementary materials).

As shown in Fig. 5a, the parabolic Hagen-Poiseuille flow is observed in slit nanochannels with varied pore sizes. In the non-swelling group of simulations, the simulated velocity profiles match well with those calculated from the Hagen-Poiseuille equation when ε_{gs}^* is typically above 5.7, proving the model's fidelity in simulating pressure-driven viscous flow. Apart from swelling, it is found that gas slippage can be achieved by decreasing the gas-solid interaction parameter ε_{gs}^*, which also controls the gas-solid affinity at pore walls. This feature facilitates the simulation of enhanced gas transport under nano-confined conditions. Fig. 5a illustrates that faster velocity profiles deviating from the Hagen-Poiseuille equations can be obtained when the gas-solid interaction ε_{gs}^* is reduced to some specific range at 1–4. On the other hand, increasing ε_{gs}^* always leads to a higher adsorption density at the pore walls as shown in Fig. 5b. The consistent density distributions at the surfaces of the three slit pores indicate that the shrinking pore size does not affect the gas slippage at pore walls. For validation purposes, a separate all-atomic MD simulation of CO_2 adsorption has been conducted in a 4 nm overmature kerogen slit pore at ~15 MPa (Figs. S2 and S3 in the supplementary materials). Although the pore size is not directly comparable to the 35.4–123.9 nm pores in CGMD, the normalized density at pore walls in the CGMD simulations (1.2–2.3) is similar to that reported in the MD slit pore simulation (1.8–2.6). This suggests a consistent distribution of adsorbed and bulk CO_2 in

nanochannels across the models of two scales, and that the CO_2 adsorption peak can be well captured in the CGMD model.

The swelling effect on the velocity profile in the $Z^* = 3.5$ slit pore is illustrated in Fig. 6a. As sorption-induced swelling is increased by adjusting ε_{gs}^*, the size of the slit nanochannel reduces, which constrains the available space for gas transport. Nevertheless, the velocity profiles in the reduced slit pores can still be described by the Hagen-Poiseuille equation with a new pore size selected as a fitting parameter. By plotting the increase of CO_2 gas particles as a function of time in the right reservoir, the mass flux of gas passing through the deformed slit pore can be calculated from the fitted slope after the steady flow has reached. Permeability is further calculated from the mass flux based on Darcy's law

$$K_a = \frac{Q\mu}{\rho A \nabla P} \tag{8}$$

where Q is the mass flux, μ is the viscosity, ρ is the gas density, A is the cross-section area, and ∇P is the pressure gradient. A linear relationship between permeability and pore size is generally observed as shown in Fig. 6b with respect to varying swelling ratio generated by turning up ε_{gs}^*. It is noticeable from the figure that the gas permeability has significantly dropped when the gas-solid interaction is larger than 6.2, or equivalently 12.5 % of solid swelling (nominal swelling ratio measured from the solid sphere as in Fig. 3c). In comparison, the gas permeability remains unaffected with the increased gas-solid interaction from $\varepsilon_{gs}^* = 5.7$ to 6.2 in the non-swelling case. This suggests that the obtained gas transport reduction is mainly attributed to the pore size contraction due to solid swelling instead of elevated gas-solid affinity at pore walls. Furthermore, no significant flux is obtained across the nanochannel as the nominal swelling ratio increases to 18.3 % at $\varepsilon_{gs}^* = 7$ according to Fig. 6b. The apparent gas permeability is reduced to nearly zero in the small-sized pores, indicating a full closure of the slit pore. By comparing the relative difference between the deformable and non-deformable simulation groups, the permeability reduction ratio from
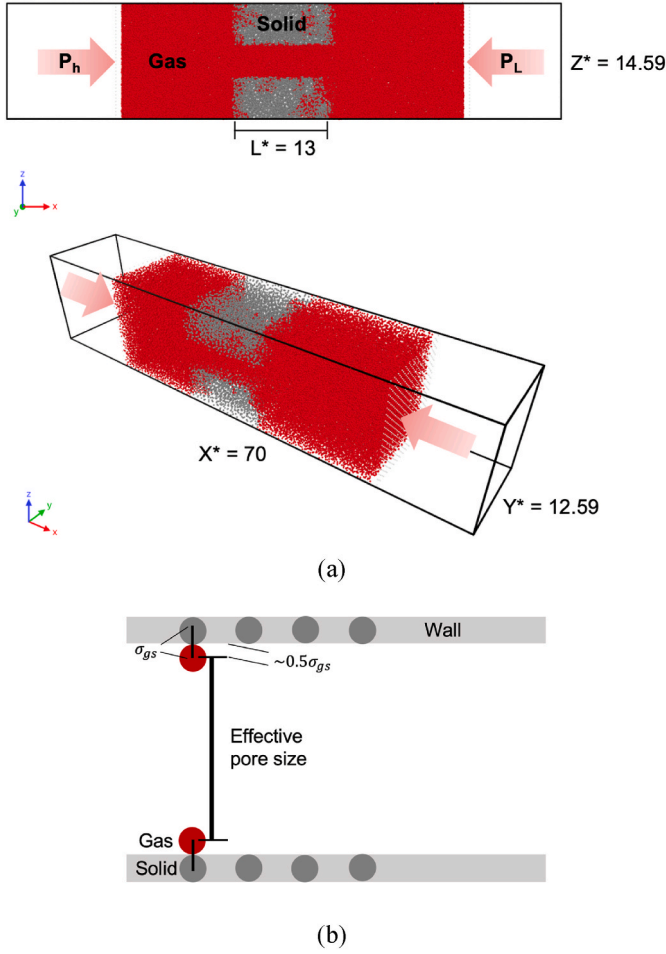
Fig. 4. Illustrations of (a) pressure-drive flow in a deformable slit pore and (b) the effective pore size. High (P_h) and low (P_L) pressure gas reservoirs at the ends are controlled by two pistons that impose forces on the gas particles. Periodic boundary conditions are applied in all the directions.

swelling ($\Delta K_a / K_a$) is obtained as a function of the slit pore size as in Fig. 6c. It can be inferred that solid swelling causes a greater relative change in small-sized pores while its impact smooths out in large pores.

3.3. Gas transport through particle-based porous media

Gas transport through a spherical particle-based porous media is considered in this section. A spherical particle ($d_p^* = 6$) cut from the simulation box containing the solid structure has been replicated four times and randomly placed into a new box as in Fig. 7a. Periodic boundary conditions are applied in all three directions. Using the same method as described in Section 3.2, a pressure-driven flow is generated in the x-direction as controlled by two pistons. The average gas pressure is 15 MPa and the pressure drop is 0.75 MPa. Approximately 5–40 % of swelling is introduced to the solid spheres by varying the gas-solid interaction ε_{gs}^* between 5.7 and 8. Fig. 7b shows the x-direction velocity profile across the region of interest (ROI). The observation indicates that as the swelling ratio increases, there is a noticeable decrease in the maximum velocity across the pore space. This reduction becomes particularly significant when the swelling ratio exceeds 12.5 %. Fig. 7c shows the normalized mass flux passing through the porous medium as a function of swelling. When there is 40 % swelling, the mass flux is almost reduced by half. The measured porosity decreases linearly with the solid swelling ratio, aligning well with the theoretical calculations.

The gas permeability is further calculated from the mass flux and

analyzed with the Kozeny-Carman equation[43]

$$K = \frac{d_p^2 n^3}{36\kappa(1-n)^2} \tag{9}$$

where d_p is the diameter of the spherical solids, n is the porosity, and κ is the Kozeny constant. Fig. 7d shows the comparison between the simulated permeability and the calculation from the Kozeny-Carman equation with $\kappa = 11.2$. It can be seen that the simulated permeability generally follows the trend of the Kozeny-Carman equation. However, some deviations are observed as porosity decreases. This may be due to the reason that the same d_p is used for the permeability calculations. As swelling occurs, d_p also increases, and therefore, the actual permeability should be higher than the calculations presented here. Porosity is related to swelling as

$$n = 1 - (1 - n_0)(1 + S) \tag{10}$$

Therefore

$$S = \frac{1-n}{1-n_0} - 1 \tag{11}$$

where n_0 is the initial porosity before swelling and S is the swelling ratio. The solid sphere size after swelling is expressed as

$$d_p = d_{p0}(1 + S)^{\frac{1}{3}} \tag{12}$$

where d_{p0} is the initial solid sphere size before swelling. Substituting Eqs. (11) and (12) into (9), we obtain

$$K = \frac{d_{p0}^2 \, n^3}{36\kappa(1-n)^{\frac{4}{3}}(1-n_0)^{\frac{2}{3}}} \tag{13}$$

The modified Kozeny-Carman equation is plotted in Fig. 7d for comparison. It is seen that Eq. (13) outperforms Eq. (9) with the swelling effect included. In Fig. S4 of the supplementary materials, we have further attempted to use the modified Kozeny-Carman equation to describe the experimental data from micromodels coated with clay.[44] The modified equation captures the general trend of permeability evolution as porosity decreases during clay swelling. However, there are deviations when the porosity becomes small. This is possibly because the clay content is only 10 % in their experiments, while our equation assumes the full solid particles swell homogeneously. Moreover, the micromodels also used square solid particles instead of spherical ones. Experiments with controlled conditions can be performed to validate further and improve this modified equation.

3.4. Summary and discussion

In this section, three case studies have been performed to show the CGMD model's ability to simulate sorption-induced swelling and gas transport in swelling porous media. It is found that sorption-induced swelling up to 130 % can be generated by controlling the two gas-solid LJ interaction parameters ε_{gs}^* and σ_{gs}^*, which is proportional to the amount of surface adsorbed gas. Subsequently, the CGMD model is used to investigate how solid swelling affects gas permeability in the slit nanochannels and spherical particle-based porous media. It is observed that setting $\varepsilon_{gs}^* \in [1, 4]$ can result in an enhanced gas velocity due to gas slippage while setting $\varepsilon_{gs}^* \in [5.7, 8]$ (nominal swelling ratio at 5–40 %) shrinks the available pore space and reduces gas permeability. A higher permeability drop is observed in small-sized pores, as 5.4 % of swelling can cause a permeability drop up to ~70 % in the 35.4 nm pore. In the spherical particle-based porous media, the mass flux is decreased by ~50 % with a porosity change of only 0.1. Results from channel flow simulations are validated against the macroscopic Hagen-Poiseuille equation when gas transport is dominated by viscous flow at $\varepsilon_{gs}^* > 4$. The relationship between permeability and porosity in the particle-
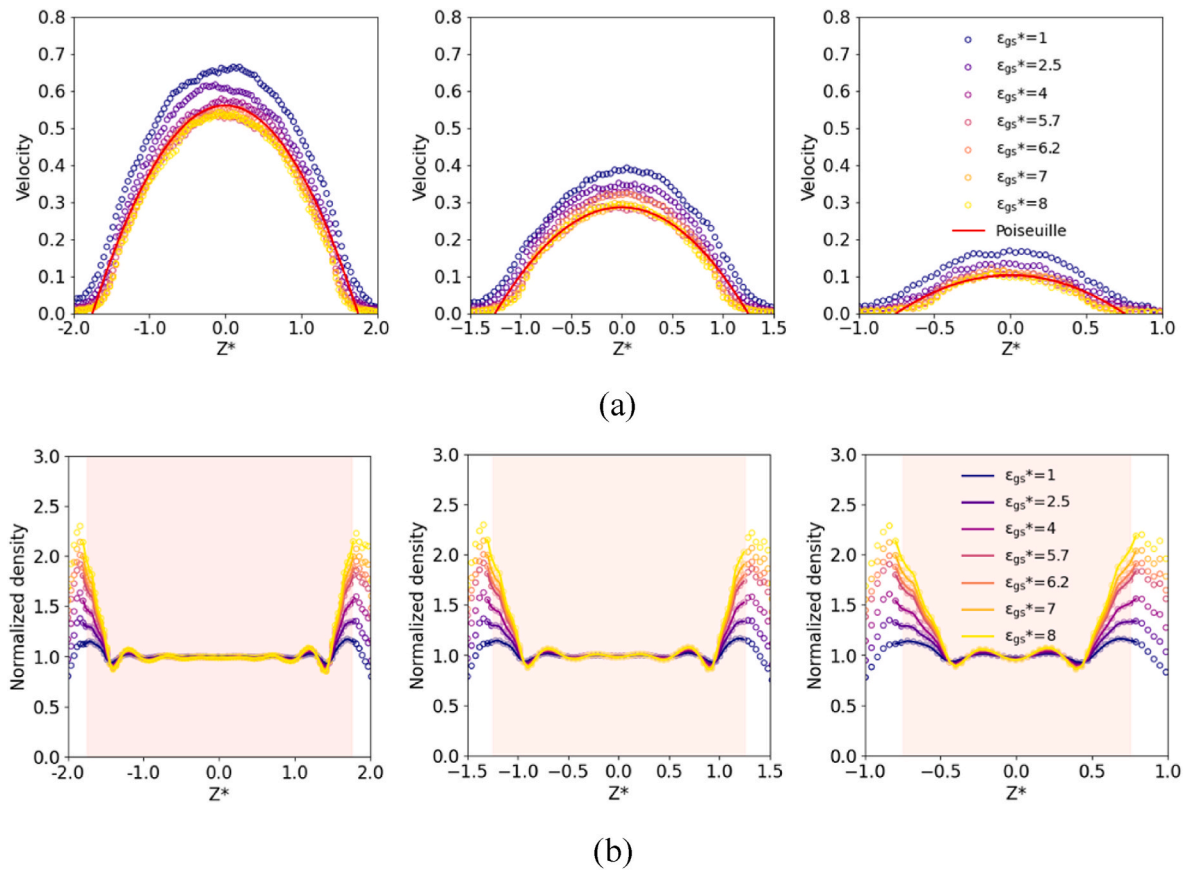
(a)

(b)

Fig. 5. Dimensionless (a) velocity and (b) density profiles across slit nanochannels at $Z^* = 3.5$, 2.5, and 1.5 with varying gas-solid interactions ε_{gs}^*. As the strength of gas-solid interaction impacts both gas slippage and swelling, the solid phase is kept rigid to isolate the effect of gas slippage since no deformation is allowed at this time. The velocity profile calculated by the Hagen-Poiseuille equation is shown as the red curve for comparison. The density profiles are normalized by the bulk gas density at $P = 15$ MPa and $T = 333.15$ K. The shaded area denotes the effective pore size where gas flow occurs. (For interpretation of the references to color in this figure legend, the reader is referred to the Web version of this article.)
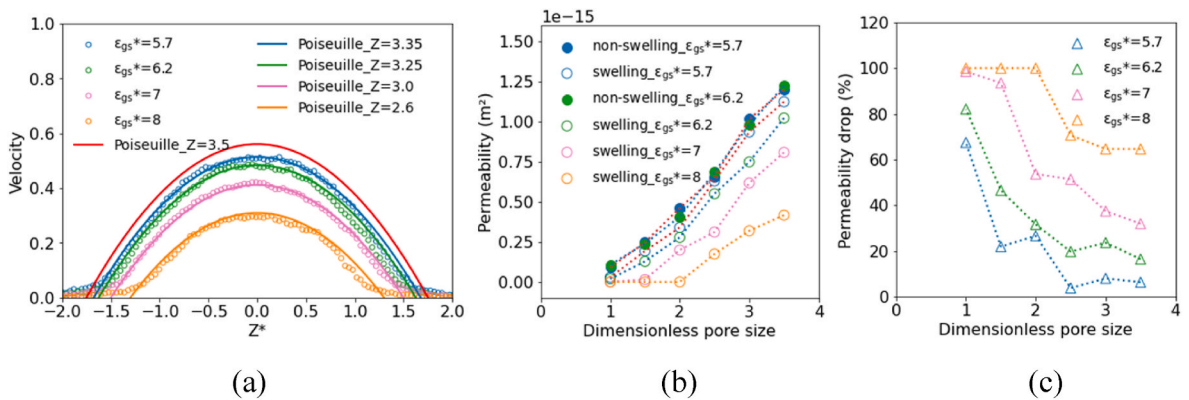

(a)   (b)   (c)

Fig. 6. (a) The development of velocity profiles as swelling is increased by tuning ε_{gs}^* from 5.7 to 8, corresponding to 5.4 %, 12.5 %, 18.3 %, and 39.9 % nominal swelling as measured from the solid sphere, respectively. The red curve shows the velocity profile calculated by the Hagen-Poiseuille equation at $Z^* = 3.5$. (b) The apparent gas permeability as a function of slit pore size with varying ε_{gs}^*. (c) The permeability reduction ratio from solid swelling as a function of slit pore size with varying ε_{gs}^*. (For interpretation of the references to color in this figure legend, the reader is referred to the Web version of this article.)

based porous media is validated against the Kozeny-Carman equation. However, solid swelling leads to minor deviations as the spherical solid diameter evolves. Modifying the Kozeny-Carman equation by including the particle size change due to solid swelling can better match with the simulation data. The gas-solid coupling method within the CGMD framework can be extended to more complex porous structures to investigate microscale gas transport. The modeling results are discussed

based on the gas transport under the steady state. If further calibrated against the swelling kinetics, the CGMD model presented here can be potentially used to study the time-evolving dynamic behavior of gas transport in swelling porous media. In addition, the current DPD model is not able to accurately reproduce a wide range of the non-linear CO_2 EOS with a general set of parameters. Future work could modify the DPD force terms to achieve better agreement.
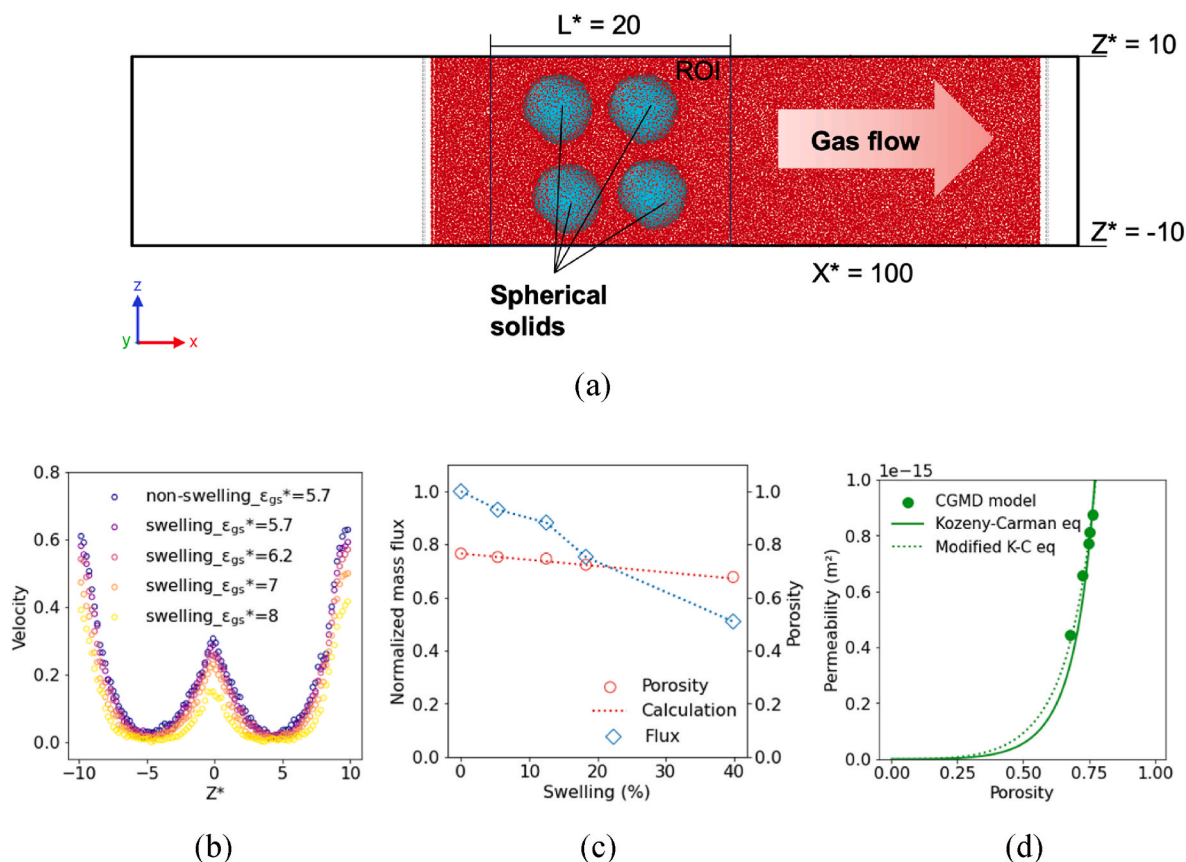
Fig. 7. (a) Illustration of gas transport through a deformable porous medium composed of four spherical solids. The y-direction dimension Y* = 9. (b) Velocity profiles across the porous medium with varying gas-solid interactions ε_{gs}^{*} controlling solid swelling. (c) Normalized mass flux and porosity as a function of solid swelling ratio. The dotted red line shows the theoretical calculations for porosity. (d) Permeability as a function of porosity and comparison with the Kozeny-Carman equation. (For interpretation of the references to color in this figure legend, the reader is referred to the Web version of this article.)

4. Conclusions

In this study, we have developed a novel CGMD approach to modeling gas transport in swelling porous media. The solid model comprises bead-spring chain networks to mimic kerogen's soft and amorphous nature with the ability to swell upon gas adsorption. Solid-solid, gas-gas, and gas-solid interactions are described by the FENE, DPD, and LJ potential functions, respectively. The Young's modulus of solid and the density and viscosity of gas are determined to match with kerogen and CO_2 properties, respectively. We have demonstrated the bead-spring chain networks model's ability to simulate a wide range of sorption-induced swelling and to couple with gas transport in both nanochannels and particle-based porous media within the CGMD framework. It is found that decreasing the gas-solid interaction gives rise to gas slippage while increasing the interaction leads to higher surface adsorption and solid swelling. Results from channel flow and particle-based porous media simulations show that a moderate level of swelling can significantly reduce permeability. Our CGMD model provides a straightforward way to simulate the coupling between fluid flow and solid deformation in different types of porous media. It can potentially be adapted to complex pore networks and is easily extensible to include more fluid phases or components.

CRediT authorship contribution statement

Jian Wu: Writing – original draft, Visualization, Validation, Methodology, Investigation, Formal analysis, Data curation, Conceptualization. **Yixiang Gan:** Writing – review & editing, Supervision, Conceptualization. **Pengyu Huang:** Writing – review & editing,

Methodology, Conceptualization. **Luming Shen:** Writing – review & editing, Supervision, Resources, Project administration, Funding acquisition, Conceptualization.

Declaration of competing interest

The authors declare that they have no known competing financial interests or personal relationships that could have appeared to influence the work reported in this paper.

Data availability

Data will be made available on request.

Appendix A. Supplementary data

Supplementary data to this article can be found online at https://doi.org/10.1016/j.ijrmms.2024.105918.

References

1. Mo CJ, Navarini L, Liverani FS, Ellero M. Modeling swelling effects during coffee extraction with smoothed particle hydrodynamics. *Phys Fluids.* 2022;34(4), 043104. https://doi.org/10.1063/5.0086897.

2. Matias AFV, Coelho RCV, Andrade JS, Araujo NAM. Flow through time-evolving porous media: swelling and erosion. *J Comput Sci-Neth.* 2021;53, 101360. https://doi.org/10.1016/j.jocs.2021.101360.

3. Williams CD, Carbone P, Siperstein FR. In silico design and characterization of graphene oxide membranes with variable water content and flake oxygen content. *ACS Nano.* 2019;13(3):2995–3004. https://doi.org/10.1021/acsnano.8b07573.

4. Kanduč M, Kim WK, Roa R, Dzubiella J. How the shape and chemistry of molecular penetrants control responsive hydrogel permeability. *ACS Nano.* 2020;15(1): 614–624. https://doi.org/10.1021/acsnano.0c06319.

5. Sharifipour M, Pourafshary P, Nakhaee A. Study of the effect of clay swelling on the oil recovery factor in porous media using a glass micromodel. *Appl Clay Sci.* 2017; 141:125–131. https://doi.org/10.1016/j.clay.2017.02.020.

6. Bui BT, Tutuncu AN. Modeling the swelling of shale matrix in unconventional reservoirs. *J Petrol Sci Eng.* 2018;165:596–615. https://doi.org/10.1016/j.petrol.2018.01.043.

7. Wang SG, Elsworth D, Liu JS. A mechanistic model for permeability evolution in fractured sorbing media. *J Geophys Res Solid Earth.* 2012;117, B06205. https://doi.org/10.1029/2011JB008855.

8. Zhou JP, Tian SF, Zhou L, et al. Experimental investigation on the influence of sub- and super-critical CO2 saturation time on the permeability of fractured shale. *Energy.* 2020;191, 116574. https://doi.org/10.1016/j.energy.2019.116574.

9. Wu J, Huang P, Maggi F, Shen L. Molecular investigation on CO_2-CH_4 displacement and kerogen deformation in enhanced shale gas recovery. *Fuel.* 2022;315, 123208. https://doi.org/10.1016/j.fuel.2022.123208.

10. Mou XZ, Chen ZQ. Pore-scale simulation of fluid flow through deformable porous media using immersed boundary coupled lattice Boltzmann method. *Transport Porous Media.* 2021;140(3):743–762. https://doi.org/10.1007/s11242-021-01558-6.

11. Sweijen T, Hassanizadeh SM, Chareyre B. Unsaturated flow in a packing of swelling particles; a grain-scale model. *Adv Water Resour.* 2020;142, 103642. https://doi.org/10.1016/j.advwatres.2020.103642.

12. Wu TH, Firoozabadi A. Effect of microstructural flexibility on methane flow in kerogen matrix by molecular dynamics simulations. *J Phys Chem C.* 2019;123(17): 10874–10880. https://doi.org/10.1021/acs.jpcc.8b12328.

13. Wu J, Shen LM, Huang PY, Gan YX. Selective adsorption and transport of CO2-CH4 mixture under nano-confinement. *Energy.* 2023;273, 127224. https://doi.org/10.1016/j.energy.2023.127224.

14. Ho TA, Wang Y, Ilgen A, Criscenti LJ, Tenney CM. Supercritical CO2-induced atomistic lubrication for water flow in a rough hydrophilic nanochannel. *Nanoscale.* 2018;10(42):19957–19963. https://doi.org/10.1039/C8NR06204H.

15. Chang Y, Xiao S, Ma R, Wang X, Zhang Z, He J. Displacement dynamics of trapped oil in rough channels driven by nanofluids. *Fuel.* 2022;314, 122760. https://doi.org/10.1016/j.fuel.2021.122760.

16. Chang Y, Xiao S, Ma R, Zhang Z, He J. Atomistic insight into oil displacement on rough surface by Janus nanoparticles. *Energy.* 2022;245, 123264. https://doi.org/10.1016/j.energy.2022.123264.

17. Liu L, Zhao Y, Luo M, Zhang L, Aryana SA. Bridging adsorption behavior of confined CH4-CO2 binary mixtures across scales. *Fuel.* 2023;354, 129310. https://doi.org/10.1016/j.fuel.2023.129310.

18. Song Y, Liu T, Wang M, et al. Kerogen differential swelling during CO2-CH4 adsorption: mechanism and significance. *Energy Fuels.* 2023;37(7):4948–4959. https://doi.org/10.1021/acs.energyfuels.2c03965.

19. Emelianova A, Balzer C, Reichenauer G, Gor GY. Adsorption-induced deformation of zeolites 4A and 13X: experimental and molecular simulation study. *Langmuir.* 2023; 39(32):11388–11397. https://doi.org/10.1021/acs.langmuir.3c01248.

20. Potier K, Ariskina K, Obliger A, Leyssale JM. Molecular simulation of argon adsorption and diffusion in a microporous carbon with poroelastic couplings. *Langmuir.* 2023;39(27):9384–9395. https://doi.org/10.1021/acs.langmuir.3c00865.

21. Joshi SY, Deshmukh SA. A review of advancements in coarse-grained molecular dynamics simulations. *Mol Simulat.* 2021;47(10-11):786–803. https://doi.org/10.1080/08927022.2020.1828583.

22. Liu C, Branicio PS. Pore size dependence of permeability in bicontinuous nanoporous media. *Langmuir.* 2021;37(51):14866–14877. https://doi.org/10.1021/acs.langmuir.1c02615.

23. Huang P, Shen L, Gan Y, Nguyen GD, El-Zein A, Maggi F. Coarse-grained modeling of multiphase interactions at microscale. *J Chem Phys.* 2018;149(12), 124505. https://doi.org/10.1063/1.5038903.

24. Huang PY, Shen LM, Gan YX, Maggi F, El-Zein A. Numerical investigation of microscale dynamic contact angles of the CO2-water-silica system using coarse-grained molecular approach. *Comput Mech.* 2020;66(3):707–722. https://doi.org/10.1007/s00466-020-01873-7.

25. Xia YD, Goral J, Huang H, Miskovic I, Meakin P, Deo M. Many-body dissipative particle dynamics modeling of fluid flow in fine-grained nanoporous shales. *Phys Fluids.* 2017;29(5), 056601. https://doi.org/10.1063/1.4981136.

26. Rao Q, Xia YD, Li JY, Deo M, Li Z. Flow reduction of hydrocarbon liquid in silica nanochannel: insight from many-body dissipative particle dynamics simulations. *J Mol Liq.* 2021;344, 117673. https://doi.org/10.1016/j.molliq.2021.117673.

27. Xia Y, Rao Q, Hamed A, et al. Flow reduction in pore networks of packed silica nanoparticles: insights from mesoscopic fluid models. *Langmuir.* 2022;38(26): 8135–8152. https://doi.org/10.1021/acs.langmuir.2c01038.

28. Durand B. *Kerogen: Insoluble Organic Matter from Sedimentary Rocks.* Editions technip; 1980.

29. Othman A, Glatz G, Aljawad MS, Alfanan S, Alarifi SA, Al Ramadan M. Review of kerogen's geomechanical properties: experiments and molecular simulation. *ACS Omega.* 2022;7(37):32829–32839. https://doi.org/10.1021/acsomega.2c03136.

30. Ho TA, Wang Y, Criscenti LJ. Chemo-mechanical coupling in kerogen gas adsorption/desorption. *Phys Chem Chem Phys.* 2018;20(18):12390–12395. https://doi.org/10.1039/C8CP01068D.

31. Brochard L, Vandamme M, Pellenq RJM. Poromechanics of microporous media. *J Mech Phys Solid.* 2012;60(4):606–622. https://doi.org/10.1016/j.jmps.2012.01.001.

32. Nikolov S, Fernandez-Nieves A, Alexeev A. Mesoscale modeling of microgel mechanics and kinetics through the swelling transition. *Appl Math Mech.* 2017;39 (1):47–62. https://doi.org/10.1007/s10483-018-2259-6.

33. Camerin F, Gnan N, Rovigatti L, Zaccarelli E. Modelling realistic microgels in an explicit solvent. *Sci Rep.* 2018;8(1), 14426. https://doi.org/10.1038/s41598-018-32642-5.

34. Groot RD, Warren PB. Dissipative particle dynamics: bridging the gap between atomistic and mesoscopic simulation. *J Chem Phys.* 1997;107(11):4423–4435. https://doi.org/10.1063/1.474784.

35. Liu MB, Meakin P, Huang H. Dissipative particle dynamics simulation of multiphase fluid flow in microchannels and microchannel networks. *Phys Fluids.* 2007;19, 033302. https://doi.org/10.1063/1.2717182.

36. Liu M, Meakin P, Huang H. Dissipative particle dynamics simulation of pore-scale multiphase fluid flow. *Water Resour Res.* 2007;43, W04411. https://doi.org/10.1029/2006WR004856.

37. Liu MB, Liu GR, Zhou LW, Chang JZ. Dissipative particle dynamics (DPD): an overview and recent developments. *Arch Comput Methods Eng.* 2014;22(4):529–556. https://doi.org/10.1007/s11831-014-9124-x.

38. Thompson AP, Aktulga HM, Berger R, et al. LAMMPS-a flexible simulation tool for particle-based materials modeling at the atomic, meso, and continuum scales. *Comput Phys Commun.* 2022;271, 108171. https://doi.org/10.1016/j.cpc.2021.108171.

39. Linstrom P, Mallard W. *NIST Chemistry WebBook, NIST Standard Reference Database Number 69.* Gaithersburg MD, 20899: National Institute of Standards and Technology; 2022.

40. Müller-Plathe F. Reversing the perturbation in nonequilibrium molecular dynamics: an easy way to calculate the shear viscosity of fluids. *Phys Rev.* 1999;59(5):4894. https://doi.org/10.1103/PhysRevE.59.4894.

41. Stukowski A. Visualization and analysis of atomistic simulation data with OVITO–the Open Visualization Tool. *Model Simulat Mater Sci Eng.* 2009;18(1), 015012. https://doi.org/10.1088/0965-0393/18/1/015012.

42. Yu XR, Li J, Chen ZX, et al. Determination of CH4, C2H6 and CO2 adsorption in shale kerogens coupling sorption-induced swelling. *Chem Eng J.* 2021;410, 127690. https://doi.org/10.1016/j.cej.2020.127690.

43. Carman PC. Fluid flow through granular beds. *Chem Eng Res Des.* 1997;75:S32–S48. https://doi.org/10.1016/S0263-8762(97)80003-2.

44. Sharifipour M, Nakhaee A, Pourafshary P. Model development of permeability impairment due to clay swelling in porous media using micromodels. *J Petrol Sci Eng.* 2019;175:728–742. https://doi.org/10.1016/j.petrol.2018.12.082.